SAND2023-05120C

JSAE 20239138

SAE 2023-YY-YYYY

Investigating molecular decomposition via high-speed laser-induced Rayleigh scattering

Julien Manin and Kevin Wan

Sandia National Laboratories

ABSTRACT

Molecular decomposition is a key chemical process in combustion systems. Particularly, the spatio-temporal information related to a fuel's molecular breakdown is of high-importance regarding the development of combustion models and more specifically about chemical kinetic mechanisms. Most experiments rely on a variety of ultraviolet or infrared techniques to monitor the fuel breakdown process in 0-D type experiments such as those performed in shock-tubes or rapid compression machines. While the information provided by these experiments is necessary to develop and adjust kinetic mechanisms, they fail to provide the necessary data for applied combustion models to be predictive regarding the fuel's molecular breakdown.

In this work, we investigated the molecular decomposition of a fuel by applying high-speed planar laser Rayleigh scattering (PLRS). The experiments were performed in the vaporized region of initially liquid sprays of n-dodecane injected in an optically-accessible constant-volume vessel at temperature and pressure conditions relevant to compression ignition engines. The sensitivity of Rayleigh scattering to the molecular cross-section enables the diagnostic to track the mixing of the fuel and oxidizer, and also detect the time and location where the injected fuel decomposes into smaller species. We also explored the ability for PLRS to detect other molecular processes such as ignition or other species growth as a result of hydrocarbon combustion. The results indicate that molecular breakdown occurs first in leaner regions, on the jet periphery, and that it shortly precedes the first appearance of low temperature reactions, as measured via high-speed laser-induced fluorescence of formaldehyde. It was demonstrated that PLRS is able to detect heat release, providing information about ignition characteristics. Similarly, and under certain conditions, a strong rise in Rayleigh scattered signal was attributed to the formation and growth of soot particles. This work developed new ways to detect important combustion processes by applying high-speed PLRS.

INTRODUCTION

A growing number of alternatives are being proposed and developed to decarbonize sectors that have traditionally relied on combustion to generate power, such as transportation, power generation and many more. Mostly driven towards electrification, advances in electric motors, but maybe more importantly about battery technologies, have changed the perspective and our reliance on combustion. Yet, some sectors are considered more challenging to be powered by electric batteries and motors, and are as such, more resistant to electric-based technologies. Compression-ignition engines for off-road vehicles or aircraft engines are two of the transportation systems that definitely fit in that "hard-to-electrify" category.

Recent forecasts predict that as light-duty vehicles are transitioning to electric-based platform, medium/heavy-duty transportation will become the number one source of carbon dioxide emissions in the next couple of decades [1]. Even then, these same predictions anticipate that aviation will be the main responsible for CO_2 emissions from the global transportation sector in half a century. As these systems rely on combustion for the time being, and more than likely for decades to come, this should not stop researchers from trying to minimize their impact on climate change.

Considering the history and the wealth of information and understanding available in the field of combustion research, changes can only be incremental nowadays. While this is certainly true for conventional technologies and fuels, new fuel formulations require a reevaluation of our understanding in order to develop combustion system that are optimal. Particularly, sustainable fuels present molecular structure and properties that may differ widely from standard diesel fuel [2]. In this context, it is evident that solid understanding about the fuels' chemistry and its relationship to one particular combustion technology is key to optimizing that system.

Sandia National Laboratories is a multimission laboratory managed and operated by National Technology & Engineering Solutions of Sandia, LLC, a wholly owned subsidiary of Honeywell International Inc., for the U.S. Department of Energy's National Nuclear Security Administration under contract DE-NA0003525.

Chemical reactions and kinetics are very important aspects of combustion and reliable chemical mechanisms are necessary for simulation tools to be predictive. Even with conventional fuels, kinetic mechanisms are continuously improved by experts in the field [3]. New fuels present new problems at this level, such that potentially new mechanisms need to be developed. This is why reliable data about the fuels' chemistry are needed for kineticists to develop mechanisms with appropriate chemical reaction pathways and rates. The vast majority of experimental efforts aiming at studying the molecular decomposition, or chemistry and kinetics in general, at elevated pressures, have been carried out in rapid compression machines [4] or shock tubes [5]. Rapid compression machines pressurize the gases in a single stroke, in a way similar to reciprocating engines. Shock tubes use two sections separated by a diaphragm: the driven section, containing the gas mixture to be tested and the driving section, used to induce the shock wave. The driving section is compressed to the point where the diaphragm ruptures and the shock wave propagates through the driven section, thereby heating and pressurizing the test gas. Combined with advanced diagnostics, often used in tandem with numerical tools, these experiments have been the basis for most contemporary kinetic mechanisms [6].

In combustion, reactions begin with the fuel decomposition, at which stage the parent fuel, typically the one injected as the fuel in the chamber containing the oxidizer, breaks down into smaller species [7]. While many articles are available in the literature about fuel decomposition experimental studies (e.g. Refs. [6, 8, 9], fewer report on experimental data at high pressures. At pressures relevant to modern jet or compression-ignition engine applications, Shao et al. [10] performed experiments in a shock tube to investigate the thermal decomposition and ignition characteristics of jet fuels. They used laser absorption spectroscopy in the mid to far infrared range to quantify the concentration levels of relevant species. They found that all fuels decompose into similar intermediate species such as methane and ethylene, at similar rates at low temperatures, but that ethylene was formed at a higher rate at higher temperatures. Unfortunately, they only reported pyrolysis data at a single pressure point (12 atm.), so the pressure effects cannot be evaluated.

One main difference between these experiments and real applications is that the test procedures use the fuels as premixed gas mixtures. This contrasts with actual engines, where the fuel is typically injected in liquid form. Expectedly, the injection, atomization and evaporation processes precede fuel decomposition. Tests in shock tube are difficult and performing measurements with similar levels of accuracy in more complex systems, including spray injection and related processes, is beyond most facilities' capabilities. This is likely why experimental data about molecular decomposition or quantitative chemistry processes at these conditions are extremely rare. We therefore propose an experimental approach to provide insight into the molecular decomposition of fuels injected in liquid form into environments at high pressures and temperatures. Because it is sensitive to molecules, laser-induced Rayleigh scattering, commonly called planar laser Rayleigh scattering (PLRS) appears as an appropriate tool to investigate molecular details. PLRS has been used extensively in combustion research to quantify mixture formation and temperature [11-13]. Fundamentally, the intensity of the Rayleigh signal is related to molecule size through what is typically referred to as the Rayleigh cross-section. This quantity, related to the total polarizability of the molecule strongly depends on the size of the molecule, as well as it's atomic composition. Concretely, as the parent fuel, such as a hydrocarbon breaks down into smaller species, i.e., shorter hydrocarbons, the scattered signal intensity will also drop, despite the same number of atoms. This comes from the non-linear relationship between hydrocarbons of different size classes and their respective Rayleigh cross-sections. For instance, there is approximately a factor of three between the Rayleigh cross-section for methane and ethane, but only a factor of two in carbon chain length. From a combustion perspective, the state of the mixture and its relationship to the Rayleigh scattered signal intensity should also be considered, as discussed by Pickett et al. [14].

While quantities and speciation information are out of reach for this technique, information regarding decomposition time and location can be extracted. We will also explore other processes of combustion that PLRS can inform about: expansion as a result of high-temperature heat release, or the formation of larger molecules such as polycyclic aromatics hydrocarbons. We will compare the information extracted from the high-speed Rayleigh scattering images to the standard diagnostics used to measure the respective or related quantities. The present manuscript is composed as follows. Following this introduction, the installation and diagnostic techniques are presented, along with the test conditions and the image processing methods specific to this application of PLRS. The results are presented next, along with the corresponding discussions. Finally, a summary of this work's main conclusions will be provided.

EXPERIMENTAL APPARATUS

INSTALLATION AND CONDITIONS

An optically-accessible, constant-volume pre-burn combustion vessel was used to injected high-pressure sprays of n-dodecane in pressurized and heated environments. The combustion chamber is of cubical shape, with a 108-mm characteristic dimension. A brief description about the vessel's operation follows, but details about the installation's capabilities or ambient gas compositions are available on the Engine Combustion Network website (ECN) [15]. The pressure and temperature in the vessel are achieved by spark-igniting a combustible gas mixtures composed of acetylene (C_2H_2), hydrogen (H_2), nitrogen (N_2) and oxygen (O_2). The ignition and rapid pressure and temperature rise as a result of heat release, are followed by a relatively long (several

seconds) period that we refer to as cooldown, as the heat is being transferred to the chamber's walls. A custom spark-plug system is installed in one of the chamber's corner port. Another corner port is fit with a mixing fan, turning at 1000 rpm while the vessel is being filled and during the pre-burn event. The other corner ports house the intake and exhaust valves, as well as pressure and temperature sensors. The sprays are injected when the target conditions are reached, during this cooldown period. The six faces of the cube can be equipped with metal ports or optical accesses, depending on the injection and optical configurations. In the current configuration, one side metal port is used to host the injector, which is mounted in the center of the port. The sprays are therefore injected horizontally, penetrating into the chamber as free sprays, away from surfaces, where the temperature distribution is the most uniform. The injector is actively cooled by a custom design water cooling jacket. The other three ports on the horizontal plane are equipped with large (approx. 100-mm diameter) sapphire windows. The top and bottom ports are made of metal but contain a machined cutout for specific laser windows to be installed. The windows, made of laser grade UV fused silica, allow the laser to come through a rectangular clear aperture that is approximately 79-mm long and 8-mm wide. A schematic of the vessel is given in Fig. 1, along with the optical diagnostics implemented in this work.

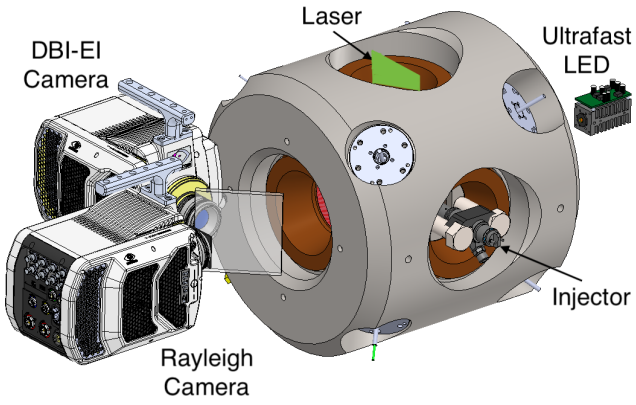

Figure 1: Constant-volume vessel and optical diagnostic equipment to perform simultaneous PLRS and DBI-EI measurements. Note that the PLRS laser sheet enters the chamber from the bottom and exit at the top.

Any source of extraneous scattering or flare interferes with quantifying the Rayleigh signal level. The laser entrance and exit windows were identified as major sources of flare because of the reflections caused by the surfaces when hit by high laser pulse energies. To minimize reflections to the imaging system, the rectangular fused silica windows were recessed into the metal ports, and internal non-reflective baffles were installed. Because of the high laser energy, windows must be kept clean to avoid damage, which would further increase reflections and flare. As such, all windows were cleaned repeatedly. In addition, most surfaces of the vessel have been coated with high-temperature, high-absorption black paint or carbon-black electro-deposition process. Reflective elements that cannot be coated, such as spark-plug electrodes, have been moved to other locations to minimize interferences, such as in the corner as described above.

The conditions targeted for these tests corresponded to a temperature variation around the ECN target Spray A case: 900 K temperature, 22.8 kg/m^3 density (60 bar) and 15-% O_2 concentration. We varied the temperature from 800 to 1200 K, but only temperatures up to 1000 K were analyzed for the purpose of this work. This was mentioned earlier, but the fuel used for the experiments reported in this manuscript was high-purity, spectroscopy-grade n-dodecane. The sprays were injected by a custom research injector. This piezoelectrically-actuated injector unit, also part of the ECN set of injectors and called Spray A-3, is equipped with a single-hole nozzle featuring a 94-μm highly-convergent (*k-factor* = 3.2) orifice [16]. The injection pressure was set to 150 MPa for these tests, and the injection timing was set to obtain a 1.5-ms long hydraulic duration. The fuel was pressurized by a high-pressure, high-precision syringe pump. The rest of the fuel system follows the ECN guidelines established more than a decade ago [15].

Specific to this campaign, the constant-volume chamber was equipped with a fast-action injector cover. Mounted to one corner of the chamber, a pneumatic-actuated lever would shield the nozzle during the pre-burn process and be moved away shortly before injection. This shield was motivated by past attempts, which showed contamination of the early injection stages presumably because of reactions happening in the nozzle mini-sac volume as a result of the pre-burn process. The contamination would be in the form of small particles (but still much larger than molecules), possibly soot, and would render all measurements invalid due to the high scattered intensity from these particles. By shielding the injector during the pre-burn process, the sprays were mostly free of such detrimental particle contamination. We speculate that the pre-burn flame was quenched and that no prejudicial chemical reactions were occurring in the nozzle prior to injection.

DIAGNOSTICS AND METHODS

Planar laser Rayleigh scattering setup

The PLRS system implemented in this study was tailored to provide time-resolved quantitative measurements of mixture fraction for vaporized sprays under high-pressure conditions. Given the reacting conditions applied here, mixture fraction can only be quantified over a very small time period. However, the procedures were the same as the non-reacting experiments, the goal being to record reliable Rayleigh scattering signal intensities as was possible under the current conditions. The system relies on a high-power, high-speed pulse-burst laser (Spectral Energies QuasiModo) and a high-speed camera (Vision Research Phantom v2512). The Nd:YAG laser fundamental was doubled to obtain a radiation wavelength of 532 nm. The laser system was set to

produce about 40 mJ/pulse at the experimental repetition rate of 70 kHz. The burst duration was set to 5.5 ms, comfortably longer than the 1.5-ms hydraulic injection duration, as mentioned earlier.

The beam was transmitted to the spray vessel using 532-nm laser-specific mirrors and anti-reflection coated fused silica or BK-7 cylindrical lenses. A -40-mm lens and a 300-mm one arranged in a Galilean telescope to expand and collimate the beam, effectively forming a sheet. Finally, a 750-mm lens was used to focus the beam and obtain a thin laser sheet at the measurement volume. With this setup, the laser sheet is expected to be around 300 μm thick. The laser sheet entered the spray vessel from the bottom, through the laser-grade fused silica window described earlier, exiting at the top of the vessel through another window of the same kind. The laser sheet, which was aligned with the spray axis, was set to appropriately illuminate the vaporized part of the jet, from 14.5 to 66.8 mm taken from the injector exit.

The high-speed camera used to record the Rayleigh scattered signal was synchronized with the laser and therefore also operated at 70 kHz. The sensor resolution under these settings was detector resolution of 512 x 400 pix^2, and the camera electronic shutter time was set to 2 μs. The camera was equipped with a Nikon 105 mm, f/1.8 lens and a 27.5-mm extension tube to allow for the camera to focus at the intended working distance – the goal being to maximize the system's digital resolution. The camera lens was equipped with a narrow 532-nm bandpass filter (3 nm FWHM) to reduce possible contamination from the flame's chemiluminescence or soot incandescence, as well as from external sources. The imaging system was placed approximately 300 mm from the jet, and it featured a projected pixel size of 108 μm.

Rayleigh scattering image processing

We employed similar image processing procedures to those described by the authors in previous works [17]. A first step corrects the images to minimize the effects of particles present in the experiments. While the injector cover described earlier proved to be very effective, small particles, still larger than the molecules under study act as contamination. The processing method relies on a detection algorithm and a two-stage inpainting scheme to effectively correct these interferences. With this approach, only the areas contaminated with particles are affected, leaving the rest of the image untouched. The background flare was then dynamically assessed and isolated from the Rayleigh scattered signal. The procedure uses the two-dimensional intensity distribution of the background flare acquired with an empty vessel (filled with N_2 at 1atm. in practice). A sensing region was set to measure the flare intensity during an injection event (at around 60 atm.), which was dynamically corrected based on the two-dimensional flare distribution. Next, the procedures deviate from the ones described by Manin and coworker [17] in that the simultaneous beam steering and spatio-temporal laser sheet distribution corrections are handled differently. For that, we only applied a differentiation algorithm comparing each frame during injection to the average of a few frames acquired immediately before the jet enters the field of view. While this procedure is not as effective globally as the aforementioned approach, it is more resistant to spray induced flare or related camera artefacts. In addition, it proved to be valid over the relatively short time-scales analyzed in the present study of about a millisecond.

Once the images have been corrected, the Rayleigh scattered signal intensity can be quantified. The theory behind Rayleigh scattering has been the subject of numerous articles and textbook. The scattered intensity depends on several parameters, but it can be summarized in the following application-driven expression [17] reformulated from Zhao and Ladommatos [11]:

$$I = I_0 \cdot \Omega \cdot \eta_{opt} \cdot L_{opt} \cdot N \cdot \sigma \qquad (1)$$

Equation 1 relates the molecular number density (N) and Rayleigh cross-section (σ) to the measued Rayleigh scattered intensity (I) assuming that the initial laser intensity (I_0), collection angle (Ω), global optical efficiency (η_{opt}) and optical path length (L_{opt}), are known.

While many of the parameters in Eq. 1 can be canceled out mathematically by using a reference signal, such as the Rayleigh scattered signal intensity in the surrounding gases [13], either the number density or the Rayleigh cross-section of the molecules must be known to calculate the other. The Rayleigh cross-section is commonly expressed as follows [18, 19]:

$$\sigma_\nu = \frac{24\pi^2\nu^4}{N^2}\left(\frac{n_\nu^2-1}{n_\nu^2+2}\right)F_k(\nu) \qquad (2)$$

In this expression, n is the refractive index of the molecule; ν is the wavenumber (in cm^{-1}), also used as subscript to indicates that the variable is wavelength dependent. This expression includes the King correction factor to compensate for the molecules' depolarization ratio, if applicable. The following formulation of the Rayleigh cross-section is useful to interpret the dependence of Rayleigh scattering to particle size (expressed as a diameter, d) and radiation wavelength (λ) [20]:

$$\sigma = \frac{2\pi^5}{3}\frac{d^6}{\lambda^4}\left(\frac{n^2-1}{n^2+2}\right) \qquad (3)$$

Equation 3 highlights the power to the six relationship with diameter and the power to the four relationship with radiation wavelength.

Rayleigh cross-sections for numerous molecules are known, but the cross-sections for several species relevant to the present work are not readily available. We used the method employed by Espey and Dec [12] and further refined by Manin et al. [17] to compute the Rayleigh cross-sections of the necessary species. The approach relies on the refractive index of the molecule under gaseous state, which can be calculated based on its dependence to the molar refractivity of the molecule. Molar refractivities for a large number of molecules have been measured and the values are

available in the literature. We used the molar refractivity data published by Gardiner et al. [21] and Vogel [22]. When the molar refractivity information was not available, such as for large aromatic species, we computed the molecules' molar refractivities from the bond polarizability properties published by Denbigh [23] and applied to the species' molecular structure.

The equivalent Rayleigh cross-section for mixtures composed of several molecules, we applied the following expression based on the respective mole fractions (X_i) and Rayleigh cross-sections of the molecules (σ_i) [11]:

$$\sigma = \sum_i (X_i \cdot \sigma_i) \quad (4)$$

Diffuse back-illumination extinction imaging (DBI-EI)

High-speed diffuse back-illumination extinction imaging was used to monitor the liquid extent of the spray, as well as to monitor soot formation. While assessing the liquid portion of the spray is not a focus of this work from a technical point of view, it still is a necessary information to properly setup the PLRS system. Specifically, it was used to adequately locate the limit of the laser sheet in the upstream region, to avoid elastic scattering from liquid droplets. A more interesting aspect from the DBI-EI images is about the formation of soot, to potentially correlate the soot processes to the Rayleigh scattering signal acquired simultaneously. The LED illumination and high-speed camera to record DBI-EI data are shown in Fig, 1. A detailed description of the technique and analog experimental setup is given in Ref. [24]. In its current form, it consists of an ultra-fast LED system with a high-power near-UV emitter (385-nm, 12-nm FWHM), a 150-mm focal length field lens, a custom, 100-mm diameter, 20-deg. engineered diffuser, and a high-speed camera (Vision Research Phantom v2512). The camera is equipped with a Nikon 50-mm f/1.2 objective and a 2-diopter close-up lens. A spectral bandpass filter is fit to the camera lens (centered at 400 nm, 36 nm FWHM), as well as an absorptive neutral density filter with an optical density of 1.0. The DBI-EI data were collected through the same optical access as the PLRS images. We used a dichroic beam-splitter to efficiently separate the respective image signal. The near-UV DBI-EI data were reflected to the corresponding camera, while the 532-nm Rayleigh scattered signal was transmitted through the beam splitter.

The DBI-EI system was synchronized with the PLRS setup. As such, the camera acquired images at 70 kHz, the PLRS laser frequency. The sensor operated at a resolution of 512 x 384 pix^2, and the exposure time was set to 2 μs. The system's wavelength to measure extinction was motivated by spectrally separating it from the PLRS laser excitation wavelength (532 nm), but more importantly, to minimize incandescence emitted by the hot soot particles in the reaction region. It is well known that soot incandescence, or black body radiation at the expected temperatures in the flame, would be higher at longer wavelengths than the laser radiation, but comparably low in the near-UV region. Because of the high laser illumination energy, that might still contaminate the DBI-EI image despite the spectral filtering scheme, the DBI-EI acquisition was set to record about 4 μs after the laser pulse.

While DBI-EI provides quantitative soot concentration or mass, making assumptions about the soot optical properties, such information only bears limited value in the present work. As such, we only processed the DBI-EI movies to extract extinction maps and expressed the extinction measure as KL, a commonly used metric in soot measurements, and equivalent to optical depth. KL is the product of dimensional extinction coefficient and the optical path length. It can simply be obtained by applying Bouguer's law (Eq. 5) to the extinction images, along with the appropriate corrections:

$$\frac{I}{I_0} = \exp(-KL) \quad (5)$$

In this application, and in most soot extinction applications, I is the measured intensity in the soot cloud, and I_0, the initial intensity at the same location, without the soot cloud. We applied Eq. 5 on a pixel-per-pixel basis across the DBI-EI images to provide a two-dimensional KL map of soot-driven extinction. The reader is referred to previous works on DBI-EI for conversion to soot concentration [25] or total soot mass [26].

RESULTS AND DISCUSSIONS

The first objective of this work is to investigate the capability and sensitivity of PLRS to provide information regarding molecular decomposition in high-pressure spray flames. As mentioned in the introduction, the scattered intensity is expected to drop as the parent fuel breaks down into smaller hydrocarbon species. At the same time, PLRS may be capable of detecting or monitoring other processes such as expansions (heat release) or species growth, such as the formation of polycyclic aromatics, or possibly soot formation. We begin by showing a sample image sequence of the corrected Rayleigh scattered signal for the ECN Spray A condition (900 K, 6.0 MPa, 15-% O_2 and 150 MPa injection pressure). The spray is injected from the left side of screen, and the field of view goes from about 15 to 67 mm. The time indicated in the top left corner is taken from the start of actual injection (ASOI). The intensity of the images displayed in Fig. 2 was normalized to highlight the different processes PLRS can detect or monitor, and the intensity is displayed in false color to enhance the relatively small intensity differences for some processes.

The first image of the sequence in Fig. 2 shows the jet entering the field of view. At this stage, the Rayleigh signal is very similar to that acquired during non-reacting environment, when the experiments' objective is to extract mixing quantities. With that said, we cannot affirm that no reactions have occurred already, but our data indicate that the first measurable reduction in signal intensity, coinciding with molecular breakdown, was observed at 0.24 ms ASOI for this injection event. In the second image of the sequence,

we can clearly observe that the signal level has dropped from the first image, indicative of molecular decomposition of the injected fuel. Furthermore, we see that the most pronounce reduction in intensity occurs on the edges of the jet, where the fuel concentration is lower and thus, higher mixing temperatures can be expected.

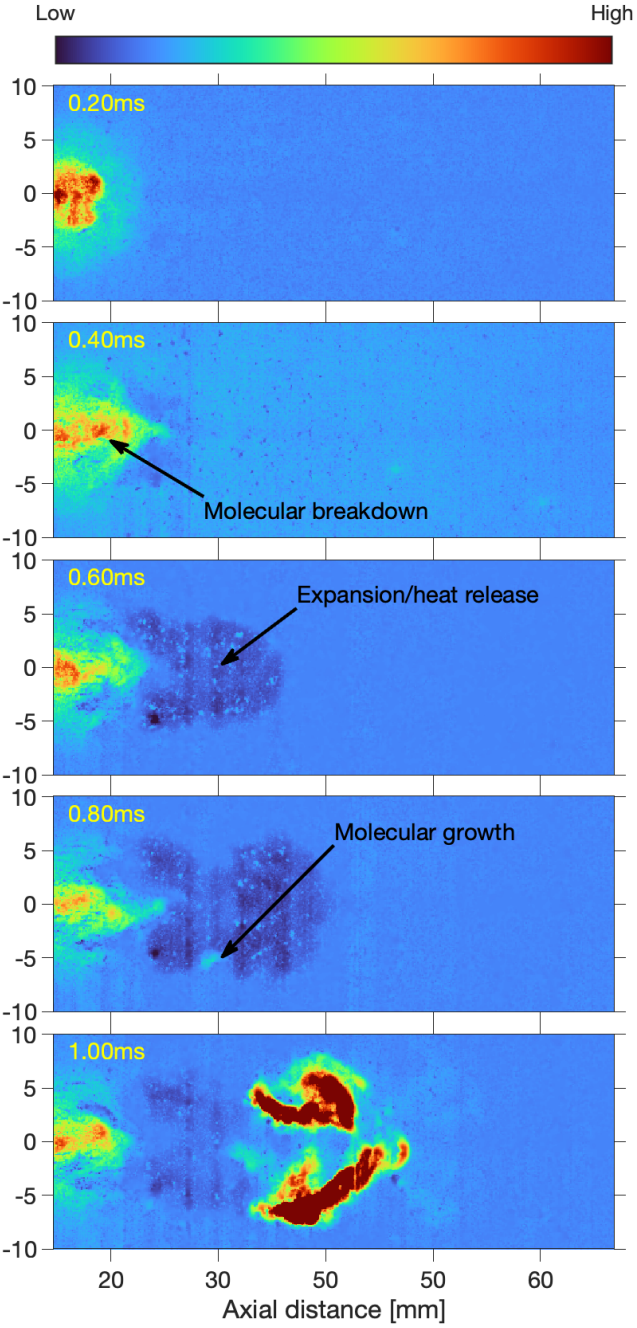

Figure 2: Time sequence of corrected Rayleigh scattered signal in false color and normalized to highlight the different identifiable processes, as labeled in the respective images. The conditions are: 900 K ambient temperature, 6.0 MPa ambient pressure, 15-% O_2 concentration and 150 MPa injection pressure.

Looking closely to the image intensity, one can see that the signal on both sides of the jet head is slightly lower than that of the ambient, which may be indicative of expansion, as a result of heat release. This is easily identified on the subsequent image in the sequence, where a larger area of the jet is now below the Rayleigh scattered signal in the ambient gases. The lower Rayleigh scattering signal in the ambient gases is a result of expansion emanating from the lower number density of gas molecules in that region. The heat release resulting from the exothermic reactions from the combustion process produces a local gas expansion by reducing the gas density induced by an increase in temperature. The relationship to the Rayleigh scattering signal intensity can be drawn from Eq. 1. The Rayleigh scattered intensity is related to the molecules' number density. The reduced gas density in the heat release region will equivalently reduce number density. Concretely, the adiabatic flame temperature for the Spray A condition featured in Fig. 2 is near 2300 K, meaning that the gas density in that region would be approximately 2.8 times lower than that of the mixture between the fuel and ambient gases at stoichiometry. Equation 1 also indicates that the Rayleigh scattered intensity is also related to the molecules' cross-sections.

While the exact molecular composition of the gas mixture in the flame region is unknown at a particular time and place in these experiments, we can estimate how sensitive the Rayleigh scattered signal can be to the expected species in that region. Closed homogeneous reactor (CHR) simulations were performed using Converge CFD to assess the fractions of the different molecules contributing to the Rayleigh scattering signal in the flame region. For this analysis, we assumed that the reaction occurred at or near stoichiometry. The boundary conditions were set to match the target conditions of this work: 900 K, 6.0 MPa and 15-% O_2. The CHR simulation results indicate that the heat release region is composed mainly of N_2, O_2, H_2O and CO_2, but we expanded the analysis to CO and OH as well, for completeness. The Rayleigh cross-section for these species are compared in the bar chart of Fig. 3. In addition, the bar chart summarizes the Rayleigh cross-sections for the molecules resulting from the decomposition of n-dodecane via oxidation, i.e., combustion.

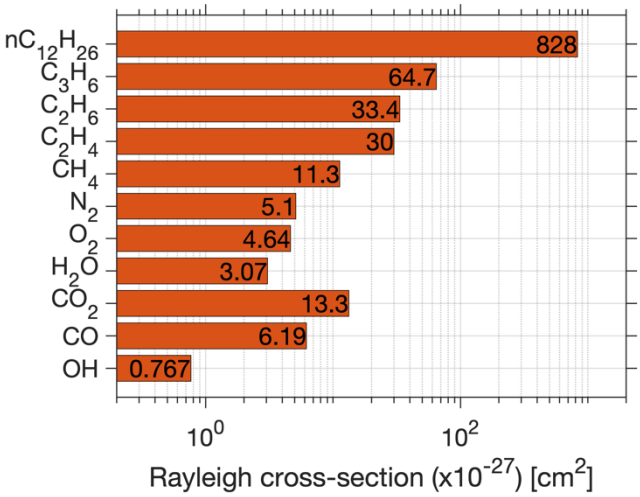

Figure 3: Rayleigh cross-sections for relevant species in the decomposition and reaction regions. The bottom axis is in logarithmic scale.

The molecules listed in the figure above came from the aforementioned CHR simulations, but the works of Herbinet et al. [9] or Smolke et al. [27] confirmed that

propene (C_3H_6), ethane (C_2H_6), ethylene, (C_2H_4) methane (CH_4) are the primary species to be expected as a result of the oxidative thermal decomposition of n-dodecane. The Rayleigh cross-sections reported in Fig, 3 were taken from measurements by Sneep and Ubachs [18] and He et al. [19], or computed from the molecules' molar refractivities, following the procedures described above.

Because the Rayleigh scattered signal intensity is directly and linearly proportional to the Rayleigh cross-section (see Eq. 1), this quantity can be used to assess the intensity from different molecules or mixtures. When stoichiometric combustion is assumed to compute the respective species' mass fractions, the weighted Rayleigh cross-section of the gases in the heat release region was calculated to be 5.78 x 10^{-27} cm^2. This is only marginally larger than that of N_2 alone, and certainly smaller than the weighted Rayleigh cross-section for the mixture of fuel and ambient gases at stoichiometry (54.6 x 10^{-27} cm^2). This means that the molecules in the heat release region are estimated to have a higher Rayleigh cross-section; yet the Rayleigh scattered signal is lower. This comparison strongly supports the argument that the reduced signal in the heat release region is the result of temperature-induced gas expansion.

Rayleigh scattering is often used to estimate the temperature of gaseous mixtures [28]. As such, attempts to estimate the temperature of the expanded region can be made. But, we believe that the relatively low signal-to-noise ratio in the flame region result in higher uncertainty levels than ideal for this estimate to be of scientific value. We should also add that the uncertainty is further increased because of lack of definite information about the concentration of species in space and time in the flame region. The error committed on the equivalent Rayleigh cross-section of the mixture during the combustion process, such as when combustion is incomplete and the environment is composed of many species, including partially decomposed molecules from the parent fuel and radicals, may be too high to justify making such estimates, even at these relatively moderate temperatures [29]. Future work will investigate this in more detail to potentially provide Rayleigh-derived temperature estimates in the flame region.

Turning to the last two images of the sequence shown in Fig. 2, one can still appreciate the heat release indicated by the lower Rayleigh scattered signal, but higher Rayleigh scattering intensity is also being measured. Specifically, much higher signal level is measured in downstream locations for the image taken a millisecond ASOI. A small region shows higher Rayleigh scattered intensity in the image taken at 0.80 ms ASOI, as indicated by the arrow labeled "Molecular growth". But, it can be difficult to make that observation from the image sequence of Fig. 2 and link it to the inception of larger species. On the other hand, the high-speed movie for that sequence clearly shows the progression from the image at 0.80 ms to the last image of the sequence (1.00 ms). Rayleigh scattering being sensitive to molecules and given its strong dependence on the molecules' cross-section. This higher Rayleigh scattered signal intensity is likely indicative of the presence of larger species, considering the relationship between molecule size (Rayleigh cross-section) and scattered intensity. Because the high-intensity region is not readily visible at low temperature (e.g., 800 K), but very apparent at 900 K, it is likely coming from large aromatics or possibly soot particles.

To investigate the likelihood of aromatics or polycyclic aromatic hydrocarbons (PAHs) being responsible for the high scattered intensity, we computed the Rayleigh cross-sections for aromatics of different sizes, from one (benzene) to four rings (pyrene). We used the method described earlier to estimate the Rayleigh cross-section of select aromatics at the wavelength of interest in this work (532 nm). The molar refractivities were computed based on the species' molecular structure and the bond polarizability properties. The injected fuel's (n-dodecane) Rayleigh cross-section is also reported in Fig. 4 for comparison. Please note that unlike Fig. 3, the Rayleigh cross-section axis uses a linear scale as opposed to a logarithmic one.

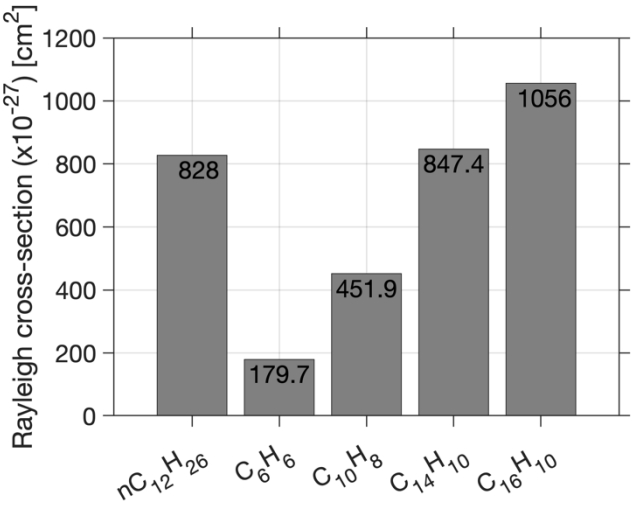

Figure 4: Comparison chart of Rayleigh cross-sections for the injected fuel and select aromatics from 1 to 4 rings.

The Rayleigh cross-sections are of the same order of magnitude for n-dodecane and moderate size or large aromatics such as phenanthrene ($C_{14}H_{10}$) or pyrene ($C_{16}H_{10}$). Naphthalene ($C_{10}H_8$) and benzene (C_6H_6) feature smaller Rayleigh cross-sections, but still within a factor 2 or 5 lower compared to that of the fuel, respectively.

Results from the CHR simulations described above can also be used to estimate the concentrations of relevant aromatics. Accounting for the mass fractions of the aromatics and their Rayleigh cross-sections suggest that it is unlikely that the high Rayleigh scattered signal observed at later timings is coming from aromatics, because of their low concentrations. For instance, the simulations predict peak benzene (C_6H_6) concentrations on the order of 1.3 x 10^{-4} at stoichiometry, but it increases by over an order of magnitude for an equivalence ratio of 2 for example. The low concentration of aromatics was confirmed by Pickett et al. [30] using a two-stage Lagrangian

reacting-jet model, which match the jet flame and mixing dynamics better than the CHR simulations. Their results demonstrate that soot precursors are mostly produced in only slightly rich regions in lifted spray flames such as probed in the present work. This comes from the statistical equivalence ratio – temperature path taken by the fuel as it mixes and reacts with the ambient gases. Their results indicate that the yield of aromatics in such regions would be on the order of 6 x 10^{-4} for pyrene ($C_{16}H_{10}$) in an environment at 1000 K and with a 15-% O_2 concentration. Lower concentration levels would therefore be expected at a lower temperature point such as the condition of Fig. 2. Even then, with this information and comparing the Rayleigh cross-sections for the aromatics listed in Fig. 5 to that of the injected fuel, it is evident that the Rayleigh scattered intensity from the aromatics would be significantly lower than that of the fuel mixture before decompositions, as shown in Fig. 2.

The conclusions that can be drawn from the above analysis are supported by companion experiments carried out with other diagnostics under identical conditions. Sim et al. [16] recently published high-speed planar laser-induced fluorescence using 355-nm excitation. While the work focused on formaldehyde (CH_2O), 355-nm laser radiation excites relatively large aromatics of sizes comparable to phenanthrene or pyrene, i.e., predominantly three- and four-ring aromatics [31]. In these experiments, and under the conditions of Fig. 2 for example, the first appearance of PAHs would be shortly past half a millisecond ASOI. This time would be substantially earlier than what the results of Fig. 2 suggest, where the late rise in Rayleigh signal is first observed at around 0.80 ms.

While the experimental data reported by Sim et al. [16] suggest that PAHs are likely to form earlier than what PLRS detects, more evidence is needed to draw definite conclusions. For instance, one can argue that the Rayleigh scattered signal intensity may only be sufficient when larger PAHs are present, rather than the moderately-sized ones probed when performing 355-nm PLIF. Additional information can be obtained from the simultaneous DBI-EI experiments performed in the present study. The high-speed DBI-EI data acquired synchronously with the PLRS images are sensitive to soot particles. If the rise in Rayleigh scattered signal intensity coincides with the first appearance of soot in the DBI-EI movies, this would provide confirmation that PLRS cannot detect PAH formation and growth under these conditions, but that it is sensitive to soot formation and growth. Figure 5 presents an image sequence extracted from the high-speed DBI-EI data, and processed to show extinction, in the form of KL (see Eq. 5). In a way similar to the image sequence of Fig. 2, the sprays are injected from the left side of the image, as such, the flame and soot field propagate from left to right. The time ASOI is also indicated in the top-left corner. Note that the timings selected for this sequence are slightly different from that of Fig. 2 in order to focus on soot formation.

The images of Fig. 5 show that the first visible soot cloud is present at approximately 0.80 ms ASOI. This compares very well with the comments made about Fig. 2, where the rise on Rayleigh scattered signal level was seen at the same time. Interestingly, the shape and location of what can be referred to as the soot cloud detected by both diagnostics are different. For instance, the soot cloud seen in the Rayleigh scattered images of Fig. 2 is at approximately 30 mm from the injector exit, and to the periphery of the jet (about 5 mm away from the spray axis). On the other hand, the DBI-EI KL map for this event and at this time indicates that the soot cloud is larger, and mostly centered on the jet axis, slightly upstream of the 40-mm mark.

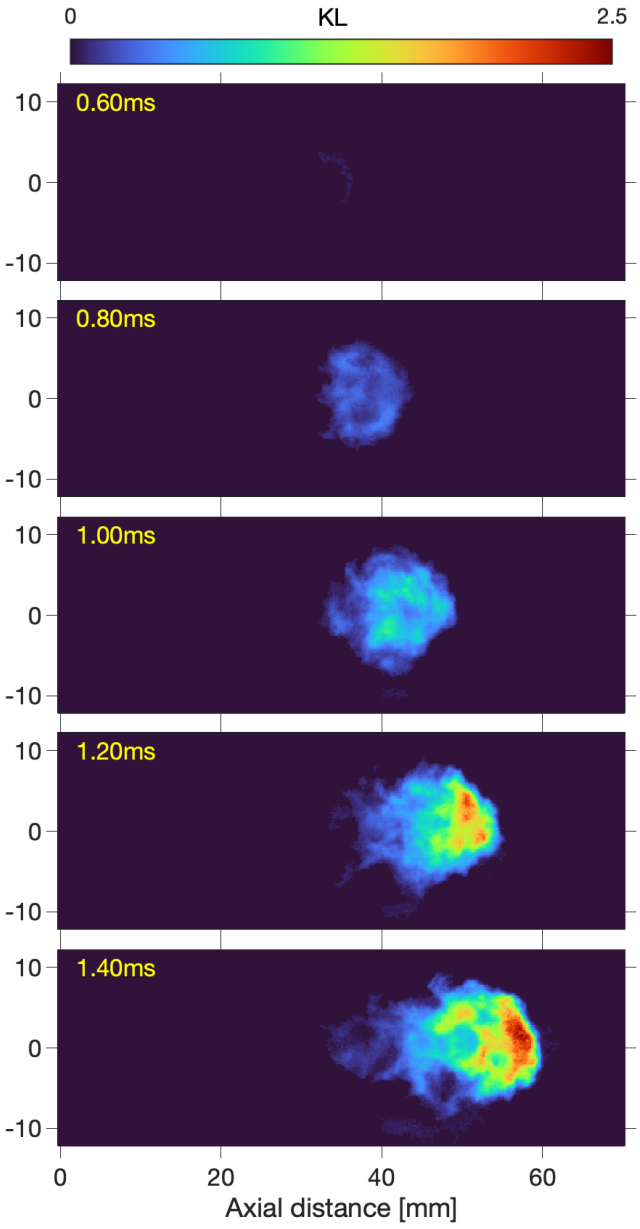

Figure 5: Time sequence of processed DBI-EI images quantifying the measured extinction (KL) from soot. This sequence was acquired simultaneously with the Rayleigh scattering sequence shown in Fig. 2. Note that the time ASOI indicated in the top-left corner is different from the sequence in Fig. 2 to focus on soot formation.

The processed high-speed movies provide great assistance to clarify the differences between the two approaches. The main difference is likely the result of

variations in the diagnostics, and particularly, the sheet illumination of PLRS compared to the path-integrated extinction of DBI-EI. PLRS relies on the laser sheet to illuminate the flame region, effectively resulting in a cut-plane taken at the plane intersecting with the jet axis. Conversely, DBI-EI is a line-of-sight technique, meaning that the extinction measured by the camera system is the result of the extinction produced by the soot field along a given light path. In a turbulent flame such as Spray A, local variations in terms of species or temperature are large. When the path-integrated technique (DBI-EI) detects a relatively smooth and centered soot field (second image of Fig. 5), the PLRS data reveal that soot only forms in the jet periphery (last image of Fig. 2). Note that applying a tomographic technique to invert the path-integrated DBI-EI 2-D extinction maps, features similar to those captured by PLRS are obtained [25]. It can be added that the measurements show that the soot field propagates into the center of the flame at later stages for this experiment.

Another way to represent the Rayleigh signal as function of time and space is by converting the time-resolved 2-D maps into a spatio-temporal representation. It is admitted that this approach is not as complete as the time-resolved 2-D data, but it has the advantage to condense the movies into a single plot. To construct the spatio-temporal plot of Rayleigh scattered signal, we took the mean intensity in the 10-mm region around the jet axis (5 mm on both sides) and plot this intensity profile as function of axial distance. Each time step or image is therefore represented as a column in the example spatio-temporal plot of Fig. 6. The intensity was adjusted and is displayed as false color to highlight the different processes. Note that the rise in Rayleigh signal intensity corresponding to the formation and growth of soot particles is above the display range used in this plot (grey region). The colormap and display range were set to emphasize the lower signal levels corresponding to fuel/air mixing, molecular breakdown and heat release.

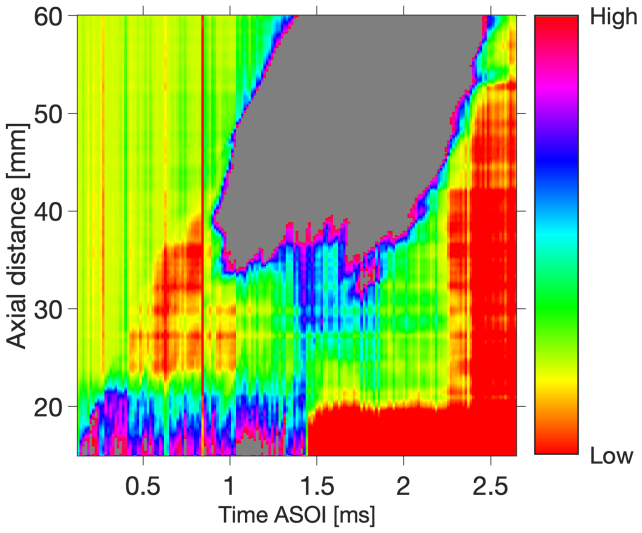

Figure 6: Spatio-temporal representation of the corrected Rayleigh scattered signal level and normalized to emphasize molecular decomposition and heat release. The conditions are the same as those in Figs. 2 and 5.

The spatio-temporal plot of Fig. 6 offers a rapid perspective on the different processes that can be identified using PLRS. Starting near the bottom left corner, the jet mixing with the ambient gases enters the field of view defined by the laser sheet in the upstream region. The jet penetrates into the chamber, but we observe a decrease in signal level shortly after, with the first noticeable drop in Rayleigh scattered level being identified near 0.25 ms ASOI. This reduction in intensity, manifested by the well-defined blue to cyan “hole” in the data around 17 to 18 mm, in a space otherwise dominated by dark blue, purple and magenta colors. The Rayleigh scattered intensity produced by the jet is continuously interrupted from that point onward and never goes past about 22 mm from the injector. Moving downstream (up in Fig. 6), the intensity turns from what corresponds to green color to yellow and red, denoting a decrease in intensity. This decrease is associated with the expansion produced by the high-temperature heat release following ignition. This area spans from approximately 23 to 40 mm downstream. Following the flame’s timeline, the heat release region transitions into the large, grey-colored region beginning near 0.90 ms ASOI, just upstream of 40 mm. This region, as we discussed above corresponds to the formation and growth of soot particles. Elastic scattering from soot particles effectively saturates the camera sensor, as anticipated given the strong size relationship with Rayleigh scattered signal intensity. But we should also note that the spatio-temporal representation of Fig. 6, as well as the time sequence of Fig. 2, are only using a limited display range, which amplifies the effect of saturation. Nonetheless, the signal remains unsaturated for a short amount of time after soot inception. Combining the Rayleigh scattered signal intensity measurements with the DBI-EI inverted soot mass fields (to extract soot concentration on the same plane as the laser sheet) may tell us more about particle size in the inception phase of soot formation. This is beyond the scope of this work, but future efforts will investigate the feasibility of using these combined diagnostics to extract particle size information. Fig. 6 also shows that soot is formed right at the end of injection (shortly before 1.5 ms in this example), as demonstrated by the vertical blue and purple area around that time. This coincides with the previously observed “flash-back”, where combustion recesses back toward the injector following the end of injection [32]. Finally, we observe heat release following the end of injection, as manifested by the red area. Initially concentrated closer to the injector, up to 20 mm downstream, the red area propagates downstream at later timings (near 2.2 – 2.3 ms ASOI). By that time, soot has mostly been oxidized and the fuel is presumably burning at lower equivalence ratio, leading to soot-free combustion.

The spatio-temporal representation may also be considered as an easier or possibly more consistent way to extract information relevant to what PLRS has to offer under these conditions. However, we repeat

that the representation of Fig. 3 was adjusted to highlight molecular decomposition and heat release, and that the specificities of data processing to obtain this plot are certainly not the most appropriate to detect soot formation. As such, we combined the analysis carried out on the spatio-temporal plots, as well as on the processed PLRS experiments to quantify onset timings for the different processes. Concretely, we assigned timings for the detection of molecular breakdown, heat release and soot from the PLRS measurements. We compared the data to related or comparable processes obtained from standard diagnostics, and the results are represented as bar charts in Fig. 7. Specifically, molecular breakdown (BD) was compared to the inception of formaldehyde (CH_2O) obtained via PLIF (c.f. Ref. [16]). Heat release (HR) from PLRS was compared to ignition delay measured by OH* chemiluminescence (data available on the ECN diesel data search utility [15]).

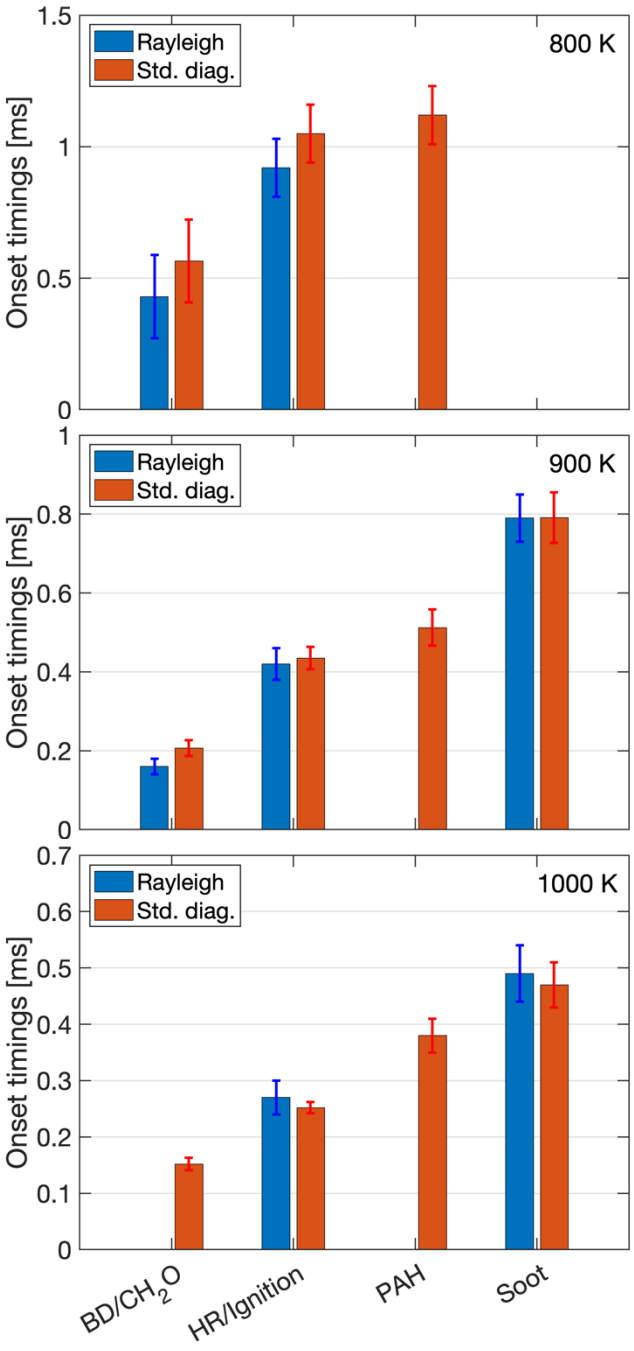

Figure 7: Onset timings for CH_2O, OH*, PAH and soot from various diagnostics and for related/comparable processes as detected via high-speed PLRS such as molecular breakdown (BD), heat release (HR) and soot formation for three ambient temperatures. The error-bars represent the experimental standard deviation.

The onset of PAHs was also reported, despite the lack of directly comparable information from the PLRS experiments, but to inform about PAH onset timing and how it relates to what we believe corresponds to soot onset from the PLRS data. The PAH onset measurements were extracted by reprocessing the experimental PLIF data reported by Sim et al. [16]. As such, and because the excitation wavelength was 355 nm, the PAH onset corresponds to aromatics of moderate sizes (mostly 3 to 4 rings), as discussed earlier in this manuscript. The soot onset was measured by processing the DBI-EI data acquired simultaneously with the PLRS experiments. It was processed following the procedures described in Wan et al. [33] to compute total soot mass in the field of view, and in which the soot onset corresponds to the time where at least 0.5 µg of soot has been produced, according to the optically-derived mass measurements. Figure 7 compiles the measurements at Spray A conditions (900 K, 6.0 MPa, 15-% O_2 and 150 MPa injection pressure), as well as two additional temperatures: 800 K and 1000 K. The error-bar displayed at the top of each bar indicates the experimental standard deviation.

Beginning with the molecular breakdown measurements, the results reported in Fig. 7 indicate that fuel decomposition shortly precedes the formation of CH_2O. This is expected, as the parent fuel (n-dodecane) needs to breakdown before formaldehyde can be formed. This observation is more a confirmation that PLRS can indeed provide insight into the molecular decomposition of the parent fuel. We should not that in this case, the parent fuel being n-dodecane, the Rayleigh cross-section is considerably larger than that of smaller species, which contributes to the diagnostic being sensitive to the molecular decomposition. PLRS may not have the sensitivity to reliably detect molecular decomposition if the parent fuel is a smaller molecule, but this remains to be determined. No PLRS data on molecular breakdown are reported for the 1000 K ambient temperature because the measurements suggest that fuel breakdown has started before the jet enters the field of view. The heat release detected by PLRS is in reasonable agreement with the ignition delay times measured via OH* chemiluminescence. We report that as the temperature increases, it becomes more challenging for PLRS to detect ignition as a result of the more subtle change in Rayleigh scattered signal level due to the temperature-induced expansion. PLRS does not inform about PAHs, but it is interesting to remark that the transition from high-temperature ignition to PAH onset, as detected by the implemented PLIF diagnostic is near constant at 0.1 ms across all temperature conditions. In fact, the measurements indicate that the PAH onset delay compared to high-temperature ignition is longer at 1000 K than it is at lower temperatures. While no soot was detected by

PLRS or DBI-EI at 800 K (despite the presence of PAHs), the onset timings are well matched at higher temperatures. The experimental data reveal that DBI-EI is a very sensitive diagnostic as it detects soot as early as in the inception phase, assuming PLRS is sensitive to incipient particles. As mentioned above, further work will attempt to confirm this and delve into extracting size information by combining PLRS and DBI-EI. In general, the measurements extracted from the PLRS data agree well with the information collected by standard, dedicated diagnostics. While more work is needed to turn PLRS into a reasonable approach to extract these measurements, the lack of alternatives to quantify molecular breakdown in such spray flame configurations makes PLRS a valuable tool, beyond its common application space.

SUMMARY AND CONCLUSIONS

We performed experiments using high-speed PLRS in high-pressure sprays under pressurized reacting conditions. We injected n-dodecane sprays into high-temperature and high-pressure environments and probed the vaporized region via PLRS. We proposed new ways to use PLRS to extract information regarding measurements of the fuel's molecular breakdown, ignition, as well as the formation of soot. The sensitivity of PLRS to molecule size or number density enables making such measurements and providing insights about the time and location of these processes.

The measurements reveal that PLRS is able to detect molecular decomposition as manifested by a reduction in scattered intensity, as expected due to the non-linear relationship between molecule size and Rayleigh cross-section. Ignition was measured using PLRS to characterize the expansion induced by the heat release following high-temperature ignition. A characteristic rise in Rayleigh scattered signal intensity was observed at later timings for the higher temperature conditions. While this rise could have been produced by molecular growth such as the formation of aromatics, the results indicate that this rise corresponds to the formation of soot. The analysis revealed that while the Rayleigh cross-section of PAHs is favorable to detection via PLRS, their number density is too low for PAHs to produce measurable Rayleigh scattered signal with this optical setup.

The information of the different processes measured via PLRS were compared to data obtained via the standard diagnostics generally employed to characterize the respective processes. The results indicate that molecular breakdown is first observed on the jet periphery, where the mixture is presumably leaner, and at higher temperature. The molecular breakdown onset measurements show that the fuel decomposes shortly prior to low-temperature reactions as measured via CH_2O PLIF. The simultaneous DBI-EI experiments, aiming at measuring soot formation, show that PLRS is equally sensitive to a standard soot diagnostic by matching the DBI-EI onset timing measurements. Future work will investigate the possibility for PLRS to quantify local temperature in the heat release region, and an attempt will be made to extract soot particle size information by combining extinction data from DBI-EI and scattering measurements from PLRS.

ACKNOWLEDGMENTS

The authors would like to thank Kyra Schmidt at Sandia National Laboratories for her dedicated support of the Spray Combustion Laboratory. This research was supported by the U.S. Department of Energy (DOE) Office of Vehicle Technologies, and was performed at Sandia Nat. Labs in Livermore, CA. Sandia is a multi-mission laboratory managed and operated by National Technology and Engineering Solutions of Sandia, LLC., a wholly owned subsidiary of Honeywell International, Inc., for the U.S. Department of Energy's National Nuclear Security Administration under contract DE-NA000352.

REFERENCES

1. International Energy Agency. World Energy Outlook 2022, IEA, 2022.
2. Schemme, S.; Samsun, R. C.; Peters, R. & Stolten, D. Power-to-fuel as a key to sustainable transport systems - An analysis of diesel fuels produced from CO2 and renewable electricity. Fuel 205, 198-221, 2017.
3. Curran, H. J. Developing detailed chemical kinetic mechanisms for fuel combustion. Proceedings of the Combustion Institute, 37, 57-81, 2019.
4. Sung, C.-J. & Curran, H. J. Using rapid compression machines for chemical kinetics studies. Progress in Energy and Combustion Science, 44, 1-18, 2014.
5. Chaos, M. & Dryer, F. L. Chemical-kinetic modeling of ignition delay: Considerations in interpreting shock tube data. International Journal of Chemical Kinetics, 42, 143-150, 2010.
6. Wang, H.; Xu, R.; Wang, K.; Bowman, C. T.; Hanson, R. K.; Davidson, D. F.; Brezinsky, K. & Egolfopoulos, F. N. A physics-based approach to modeling real-fuel combustion chemistry - I. Evidence from experiments, and thermodynamic, chemical kinetic and statistical considerations. Combust. Flame, 193, 502-519, 2018.
7. Manelis, G. B. Thermal decomposition and combustion of explosives and propellants. CRC Press, 2003.
8. McEnally, C. S.; Ciuparu, D. M. & Pfefferle, L. D. Experimental study of fuel decomposition and hydrocarbon growth processes for practical fuel components: heptanes. Combust. Flame, 134, 339-353, 2003.
9. Herbinet, O.; Marquaire, P.-M.; Battin-Leclerc, F. & Fournet, R. Thermal decomposition of n-dodecane: Experiments and kinetic modeling. Journal of analytical and applied pyrolysis, 78, 419-429, 2007.
10. Shao, J.; Zhu, Y.; Wang, S.; Davidson, D. F. & Hanson, R. K. A shock tube study of jet fuel pyrolysis and ignition at elevated pressures and temperatures. Fuel, 226, 338-344, 2018.

11. Zhao, H. & Ladommatos, N. Optical diagnostics for in-cylinder mixture formation measurements in IC engines. Prog. Energ. Combust., 24, 297-336, 1998.
12. Espey, C.; Dec, J. E.; Litzinger, T. A. & Santavicca, D. A. Planar laser Rayleigh scattering for quantitative vapor-fuel imaging in a Diesel jet. Combust. Flame, 109, 65-78, 1997.
13. Idicheria, C. A. & Pickett, L. M. Quantitative mixing measurements in a vaporizing Diesel spray by Rayleigh imaging. SAE Paper 2007-01-0647, 2007.
14. Pickett, L. M.; Manin, J.; Genzale, C. L.; Siebers, D. L.; Musculus, M. P. B. & Idicheria, C. A. Relationship between diesel fuel spray vapor penetration/dispersion and local fuel mixture fraction. SAE Paper 2011-01-0686 - SAE Int. J. Engines, 4, 764-799, 2011.
15. Engine Combustion Network. www.sandia.gov/ecn/. Sandia National Laboratories, 2023.
16. Sim, H.-S.; Maes, N.; Weiss, L.; Pickett, L. M. & Skeen, S. A. Detailed measurements of transient two-stage ignition and combustion processes in high-pressure spray flames using simultaneous high-speed formaldehyde PLIF and schlieren imaging. Proceedings of the Combustion Institute, 38, 5713-5721, 2021.
17. Manin, J.; Pickett, L. M.; Skeen, S. A. & Frank, J. H. Image processing methods for Rayleigh scattering measurements of diesel spray mixing at high repetition rate. Appl. Phys. B-Lasers O., 127, 1-19, 2021.
18. Sneep, M. & Ubachs, W. Direct measurement of the Rayleigh scattering cross section in various gases. Journal of Quantitative Spectroscopy and Radiative Transfer, 92, 293-310, 2005.
19. He, Q.; Fang, Z.; Shoshanim, O.; Brown, S. S. & Rudich, Y. Scattering and absorption cross sections of atmospheric gases in the ultraviolet--visible wavelength range (307--725 nm). Atmospheric Chemistry and Physics, 21, 14927-14940, 2021.
20. Howell, J. R.; Menguc, M. P.; Daun, K. & Siegel, R. Thermal radiation heat transfer. CRC press, 2020.
21. Gardiner Jr., W. C.; Hidaka, Y. & Tanzawa, T. Refractivity of combustion gases. Combust. Flame, 40, 213-219, 1981.
22. Vogel, A. Physical properties and chemical constitution of aliphatic hydrocarbons. J. Chem. Soc, 9, 133-142, 1946.
23. Denbigh, K. The polarisabilities of bonds - I. Transactions of the Faraday Society, 36, 936-948, 1940.
24. Westlye, F. R.; Penney, K.; Ivarsson, A.; Pickett, L. M.; Manin, J. & Skeen, S. A. Diffuse back-illumination setup for high temporally resolved extinction imaging. Appl. Optics, 56, 5028-5038, 2017.
25. Manin, J.; Pickett, L. M. & Skeen, S. A. Two-Color Diffused Back-Illumination Imaging as a Diagnostic for Time-Resolved Soot Measurements in Reacting Sprays. SAE Paper 2013-01-2548 - SAE Int. J. Engines, 6, 1908-1921, 2013.
26. Skeen, S. A. & Yasutomi, K. Measuring the soot onset temperature in high-pressure n-dodecane spray pyrolysis. Combust. Flame, 188, 483-487, 2018.
27. Smolke, J.; Carbone, F.; Egolfopoulos, F. N. & Wang, H. Effect of n-dodecane decomposition on its fundamental flame properties. Combust. Flame, 190, 65-73, 2018.
28. Dibble, R. W. & Hollenbach, R. E. Laser Rayleigh thermometry in turbulent flames. Symp.(Int.) Combust.,(Proc.), 1981.
29. Limbach, C.; Dumitrache, C. & Yalin, A. P. Laser light scattering from equilibrium, high temperature gases: limitations on Rayleigh scattering thermometry. 47th AIAA Plasmadynamics and Lasers Conference, 3381, 2016.
30. Pickett, L. M.; Caton, J. A.; Musculus, M. P. B. & Lutz, A. E. Evaluation of the equivalence ratio-temperature region of diesel soot precursor formation using a two-stage Lagrangian model. Int. J. Engine Res., 7, 349-370, 2006.
31. Zhang, Y.; Li, Y.; Wang, L.; Liu, P.; Zhan, R.; Huang, Z. & Lin, H. Investigation on the LIF spectrum superposition of gas-phase PAH mixtures at elevated temperatures: potential for the analysis of PAH LIF spectra in sooting flames. Applied Physics B, 125, 1-13, 2019.
32. Knox, B. W.; Genzale, C. L.; Pickett, L. M.; Garcia-Oliver, J. M. & Vera-Tudela, W. Combustion recession after end of injection in diesel sprays. SAE Int. J. Engines, 8, 679-695, 2015.
33. Wan, K.; Manin, J.; Sim, H.-S. & Karathanassis, I. Soot and PAH formation in high pressure spray pyrolysis of gasoline and diesel fuels. Combust. Flame, 241, 112084, 2022.

CONTACT

Julien Manin, Ph.D. Sandia National Laboratories, jmanin@sandia.gov

Kevin Wan, Ph.D. Sandia National Laboratories, kwan@sandia.gov

DEFINITIONS, ACRONYMS, ABBREVIATIONS

ASOI: After the start of injection

BD: Molecular breakdown

CFD: Computational fluid dynamics

CHR: Closed homogeneous reactor

ECN: Engine Combustion Network

DBI-EI: Diffuse back-illumination extinction imaging

FWHM: Full-width at half-maximum

HR: High-temperature heat release

KL: Optical depth (K x L)

PAH: Polycyclic aromatic hydrocarbon

PLIF: Planar laser-induced fluorescence

PLRS: Planar laser Rayleigh scattering